Advanced Materials in Wireless, Implantable Electrical Stimulators That Offer Rapid Rates of Bioresorption for Peripheral Axon Regeneration

Hexia Guo,

Department of Materials Science and Engineering, Querrey Simpson Institute for Bioelectronics, Northwestern University, Evanston, IL 60208, USA

Dom D'Andrea,

Laboratory of Regenerative Rehabilitation, Shirley Ryan AbilityLab, Chicago, IL 60611, USA

Jie Zhao,

Department of Materials Science and Engineering, Querrey Simpson Institute for Bioelectronics, Northwestern University, Evanston, IL 60208, USA

Department of Materials Science, Fudan University, Shanghai, 200433, China

Yue Xu,

Department of Biomedical Engineering, Northwestern University, Evanston, IL 60208, USA

Zheng Qiao,

Department of Materials Science and Engineering, Northwestern University, Evanston, IL 60208, USA

Lindsay E. Janes,

Department of Physical Medicine and Rehabilitation, Neurological Surgery, Division of Plastic and Reconstructive Surgery, Northwestern University, Chicago, IL 60611, USA

Nikhil K. Murthy,

Laboratory of Regenerative Rehabilitation, Shirley Ryan AbilityLab, Department of Neurological Surgery, Northwestern University, Chicago, IL 60611, USA

Rui Li,

State Key Laboratory of Structural Analysis for Industrial Equipment, Department of Engineering Mechanics, International Research Center for Computational Mechanics, Dalian University of Technology, Dalian 116024, China

Zhaoqian Xie,

State Key Laboratory of Structural Analysis for Industrial Equipment, Department of Engineering Mechanics, International Research Center for Computational Mechanics, Dalian University of Technology, Dalian 116024, China

cfranz@sralab.org, jrogers@northwestern.edu.

Zhen Song,

State Key Laboratory of Structural Analysis for Industrial Equipment, Department of Engineering Mechanics, International Research Center for Computational Mechanics, Dalian University of Technology, Dalian 116024, China

Rohan Meda,

Laboratory of Regenerative Rehabilitation, Shirley Ryan AbilityLab, Chicago, IL 60611, USA

Jahyun Koo,

Department of Materials Science and Engineering, Querrey Simpson Institute for Bioelectronics, Northwestern University, Evanston, IL 60208, USA

School of Biomedical Engineering, Interdisciplinary Program in precision Public Health, Korea University, Seoul 02841, Republic of Korea

Wubin Bai,

Department of Materials Science and Engineering, Querrey Simpson Institute for Bioelectronics, Northwestern University, Evanston, IL 60208, USA

Yeon Sik Choi,

Department of Materials Science and Engineering, Querrey Simpson Institute for Bioelectronics, Northwestern University, Evanston, IL 60208, USA

Sumanas W. Jordan,

Biologics, Shirley Ryan AbilityLab, Division of Plastic and Reconstructive Surgery, Northwestern University, Chicago, IL 60611, USA

Yonggang Huang,

Department of Civil and Environmental Engineering, Mechanical Engineering, Materials Science and Engineering, Center for Bio-integrated Electronics, Querrey Simpson Institute for Bioelectronics, Northwestern University, Evanston, IL 60208, USA

Colin K. Franz,

Laboratory of Regenerative Rehabilitation, Shirley Ryan AbilityLab, Department of Physical Medicine and Rehabilitation, The Ken and Ruth Davee Department of Neurology, Northwestern University Feinberg School of Medicine, Chicago, IL 60611, USA

John A. Rogers

Department of Materials Science and Engineering, Biomedical Engineering, Neurological Surgery, Chemistry, Mechanical Engineering, Electrical and Computer Engineering, Center for Bio-integrated Electronics, Querrey Simpson Institute for Bioelectronics, Northwestern University, Evanston, IL 60208, USA

Abstract

Injured peripheral nerves typically exhibit unsatisfactory and incomplete functional outcomes, and there are no clinically approved therapies for improving regeneration. Post-operative electrical stimulation (ES) increases axon regrowth, but practical challenges from the cost of extended operating room time to the risks and pitfalls associated with transcutaneous wire placement have prevented broad clinical adoption. This study presents a possible solution in the form of advanced bioresorbable materials for thin, flexible, wireless implant that provides precisely controlled ES

of the injured nerve for a brief time in the immediate post-operative period. Afterward, rapid, complete and safe modes of bioresorption naturally and quickly eliminate all of the constituent materials in their entirety, without the need for surgical extraction. The unusually high rate of bioresorption follows from the use of a unique, bilayer enclosure that combines two distinct formulations of a biocompatible form of polyanhydride as an encapsulating structure, to accelerate the resorption of active components and confine fragments until complete resorption. Results from mouse models of tibial nerve transection with re-anastomosis indicate that this system offers levels of performance and efficacy that match those of conventional wired stimulators, but without the need to extend the operative period or to extract the device hardware.

Graphical Abstract
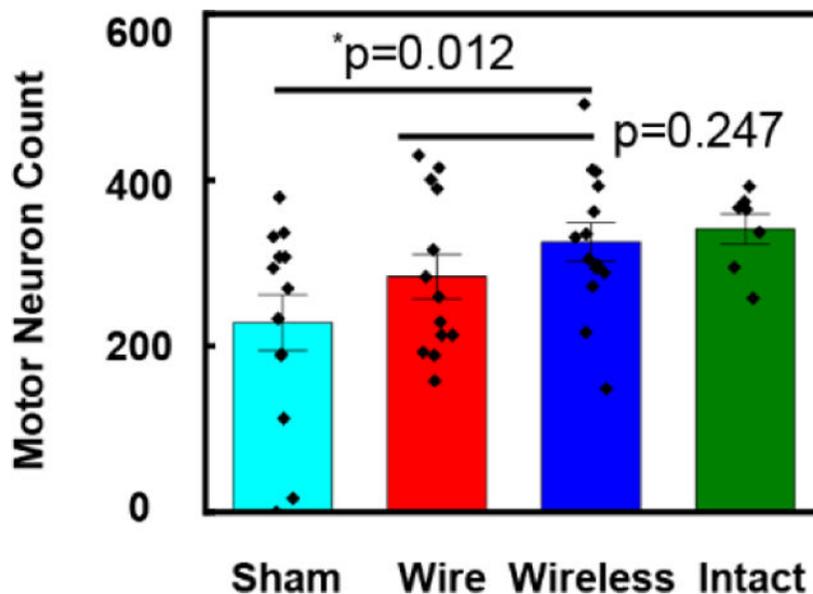
A wireless bioresorbable implant is introduced to perform electrical stimulation of injured nerve to accelerate axon regeneration. The bioimplant is based on tailored polyanhydride materials to achieve rapid bioresorption after operation. In vivo biocompatibility study supports application in animal model. Results from mouse model of tibial nerve transection demonstrate enhanced axon regeneration with electrical stimulation from this bioresorbable implant.

Keywords

biodegradable polymer; bioresorbable electronics; transient electronics; biomedical implants; electrical stimulation; peripheral axon regeneration

1. Introduction

Peripheral nerves form the basis for communicating motor and sensory information throughout the body to the central nervous system. Damage to peripheral nerves can occur from a myriad of events, including traumatic accidents such as vehicle collisions, degradation from chronic issues such as carpal tunnel syndrome, injuries in iatrogenic

fashion associated with medical procedures, or degeneration from a variety of diseases that affect the nervous system. Approximately 200,000 new peripheral nerve injury (PNI) cases occur in the USA each year,[1] and while the severity of impairment varies, the vast majority of patients get permanent functional impairments. These persistent impairments largely stem from the fact that peripheral axon regeneration is a slow and incomplete process. Full functional restoration is rare except in cases of minor and/or distal nerve injuries. Currently there are no clinical treatments to improve the speed or extent of axon regrowth besides surgical re-anastomosis or grafting, in the most extreme cases where the nerve has been completely transected. Another complication is that muscles left without neural input for extended periods of time atrophy and degrade. As a result, even if motor axons eventually reach the muscle, the window of opportunity to restore gross muscle function may end.[1c, 2] Fine motor control and skin sensibility are often permanently impaired as well.

Many in vivo and in vitro studies over the last 40 years suggest that a brief period (usually   1 hour) of low-frequency electrical stimulation (ES) applied to injured axons can accelerate the rates of sensorimotor recovery post-injury. This ES paradigm works in part by mimicking the wave of calcium ions that back-propagate along injured axons to their cell bodies, thereby stimulating increased release of brain-derived neurotrophic factor (BDNF).[3] The retrograde conduction of action potentials from the site of ES to the neuronal cell body is both necessary and sufficient to enhance axon regeneration.[4] This activation-dependent release of BDNF is crucial, as it binds to tropomyosin receptor kinase B (trkB) receptors which in turn promotes persistent pro-growth conditions.[5] Both endogenous and exogenous increases in BDNF upregulate trkB-related pro-growth signaling cascades acting at the level of transcription in the nucleus, such as phospholipase C gamma, phosphotidyl-inositol-3 kinase, and mitogen activated protein kinase/extracellular receptor kinase.[6] Additionally, trkB activation by BDNF engages at the neural growth cone, boosting synthesis of the actin and tubulin that form the regenerating neural cytoskeleton[7] and increasing their rate of transport toward the growth cone.[8] Altogether, these downstream effects of ES increase activity-dependent BDNF release and cause injured axons to cross the injury site to re-enter the distal endoneurial tube more rapidly and in greater numbers.[9]

Three, single center randomized clinical trials on post-operative ES led by Chan and colleagues show positive results. Motor unit numbers in reinnervated hand intrinsic muscles were increased by 1 hour of ES at 20 Hz following nerve decompression at the carpal tunnel[10] or cubital tunnel[11] at both early and late recovery time points. ES enhances finger sensory function 5 to 6 months postoperatively compared to controls in a patient population with complete digital nerve transection with surgical repair.[12] These trials represent encouraging progress, but further larger clinical studies involving multiple centers are necessary to demonstrate that this intervention can extend beyond a single center as well as to better characterized its functional impact in daily life activities.

The methods for ES in these trials and in most rodent models rely on intraoperative insertion of wire electrode leads into the surgical incision at the time of nerve repair. External power supplies initiate stimulation for the hour-long ES process, after which the electrodes must be carefully removed from the delicate nerve tissue. This process requires continuous attention from highly skilled surgeons and clinical neurophysiologists, and it extends the time in the

operating room, with significant additional costs and risks to the patient. These limitations frustrate the broader adoption of therapeutic applications of intraoperative ES based on conventional, wired stimulators.[13] A recent paper from our group describes a wireless, bioresorbable electronic system for post-operative ES. The results indicate improved rates of peripheral nerve functional recovery with both one-hour stimulation and intermittent stimulation over 6 days during the healing process.[14] This platform, however, requires some months to completely resorb, and during this process the implant breaks down into fragments that have the potential to disperse in an uncontrolled fashion that could lead to adverse outcomes such as inflammation.

The advances reported here eliminate these disadvantages in a system built with advanced bioresorbable materials to support the standard one-hour ES protocol and then to undergo rapid bioresorption to completely and safely eliminate the device in its entirety. A unique bilayer enclosure formed with two different bioresorbable polyanhydride enables resorption of the wireless electronics within three days, where intermediate degradation debris remains confined within a soft encapsulating capsule. The water-triggered degradation process of the inner layer of polymer releases acidic moieties, to enable accelerated dissolution of the electronic materials, and then this capsule itself resorbs over the following ten days. Comparisons of this fast-resorbing platform against the standard-of-care wired devices for ES yield quantitative data on device performance and effectiveness in promoting increased axon regeneration after nerve injury in mice.

2. Results and discussion

2.1. Fast-bioresorbable wireless electrical stimulators for peripheral nerve regeneration

The system exploits a bilayer of two different formulations of polyanhydride (PA) to encapsulate a device capable of wireless ES of a targeted nerve, with stable operation for up to 5 hours in Figure S1–2, which is sufficient to cover initial one-hour stimulation period, followed by subsequent fast rates of bioresorption to eliminate the device without residue. Figure 1a and Figure 1b present exploded and integrated schematic illustrations of the layout. The first of the two major parts of this system is a radio frequency (RF) energy harvester and electrical interconnection to the nerve. The harvester consists of two Mg coils (thickness: ~10 μm) stacked on top of one another on a polyanhydride (PA-90, ~170 μm thick, with about equivalent mole of anhydride group as Mg) substrate and spaced with a dielectric layer of partially oxidized sodium alginate (thickness: ~10 μm).[15] A diode constructed from a silicon nanomembrane (Si NM diode, ~320 nm thick) rectifies the RF power received by the coils. A second layer of polyanhydride (PA-70, ~20 μm thick, minimum thickness with uniform coating layer to avoid leakage) serves as the outer part of the encapsulating structure for Mg coils (Figure 1a). The second part is the interconnect that includes two Mg wires (width: ~340 μm, thickness: ~ 40 μm) on a substrate of poly (lactic-co-glycolic acid) (PLGA, lactide: glycolide 50:50, ~20 μm thick) with an overcoat of PLGA (~20 μm thick). One end connects to the receiver coils and other to exposed Mg electrodes (length: ~ 3 mm) on a hot-pressed PLGA cuff designed to mount around the nerve to deliver ES without parasitic electrical interaction with surrounding tissue (Figure 1b, Figure S3, and Table S1). Figure 1c shows an optical image of a complete system resting

on a fingertip and a magnified view of the exposed Mg electrodes and PLGA cuff. Figure 1d and Figure S4 summarize key RF characteristics of the assembled device. Absorption of RF power associated with biofluids and tissues at the operating frequency (~18 MHz) is negligible.[16] Figure 1d and Figure S4–5 summarize the RF properties simulated by finite element analysis, as a function of the thickness of the Mg coil. As expected, the power transfer efficiency decreases with the thickness. To fully activate the injured nerve by ES with the setup in experimental section, in practical operation, the thickness of Mg coils needs to be a few tens of micrometers to reach the threshold power. The natural rate of dissolution of Mg exposed directly to biofluids at physiological conditions is between 1 and 10 μm/day,[17] with much lower rates when encapsulated by most common bioresorbable polymers, such as PLGA. The dissolution process typically yields fragments that have the potential to move through the body in an uncontrolled manner.[14] The bilayer PA encapsulation strategy introduced here solves both issues by accelerating the dissolution of Mg via acidic degradation products that result from the dissolution of the inner layer of PA structure and by containing the dissolution fragments inside the soft capsule of the outer layer of PA structure.

Figure 1e presents chemical structures of the monomers, the synthetic reactions, and the hydrolysis processes associated with the PA reported here. Crosslinking of 4-pentenoic anhydride (4-PA), poly (ethylene glycol) (PEG) diacrylate, and pentaerythritol tetrakis(3-mercaptopropionate) (PETMP) occurs via thiol-ene photopolymerization.[18] The ene and thiol functional groups are in a stoichiometric relationship. Different ratios of 4-PA to PEG diacrylate yields PAs with different properties. Hereafter, the -xx term in PA-xx denotes the molar percentage of the ene functional group associated with 4-PA. For example, PA-90 indicates that 90% of the ene is from 4-PA and the remaining 10% is from PEG diacrylate. Additional synthetic details are in the Materials and Methods. Hydrolysis of the PA generates carboxylic acid.[18a, 18b] The resulting decreases in pH increase the rate of dissolution of Mg, to enable fast bioresorption. According to other in vitro studies, the rate of dissolution of Mg at a pH of 6.2 (~420 μm/day) is about 70 times higher than that at a pH of 7.4 (~6 μm/day).[19] Although the rate of dissolution of the Si NM decreases at a lower pH,[20] the amount of Si (~1 μg) is negligible compared to that of other key electronic materials Mg (~3 mg) and of the entire device structure (~30 mg).

2.2. In vitro and in vivo studies of degradation of polyanhydride and Mg

In vitro degradation studies of various PAs happen when immersing in phosphate buffered saline (PBS) solution at 37 °C as shown in Figure 2a–b and Figure S6. Increasing the amount of 4-PA increases the rate of degradation (Figure 2a, PA-90 and PA-80, ~27 μm/day). PA-90 becomes viscous and dramatically softens (Figure S6) with an associated loss of >50% of its mass after 12 h. In Figure 2b, the studies of changes in pH involve an equivalent polymer concentration of 1 mg/mL in PBS. The hydrolysis generates acidic products, resulting in strong decreases in pH, to reach values of ~6.0 (PA-90 and PA-80). PA-90 and PA-80 have similar hydrolysis kinetics and in the wireless stimulator PA-90 is favorable because PA-90 has a higher ratio of anhydride therefore it requires less weight of materials to react with Mg stoichiometrically after degradation, thereby reducing the materials load. The results in Figure 2a–b and Figure S6 indicate that PA-70, PA-60, and

PA-50 exhibit progressively lower rates degradation and hydrolysis (PA-70: ~10 μm/day, PA-60: ~1.7 μm/day, and PA-50: ~0.8 μm/day). PA-50 remains solid and retains ~95% of its mass after 3 days.

Reactive diffusion simulations capture the effects of water permeation and reactions with PA and underlying Mg based on experimental measurements of the degradation profiles of films of PA-90 and PA-70 film with thicknesses, and the changes in resistance of Mg layers beneath encapsulating layers of PA (Figure 2c–d and Figure S7). A single layer model of PA with an initial thickness h_{PA} in PBS solution appears in Figure S7a, to illustrate a coordinate system (oz), with the origin (o) located at the thickness midpoint and the oz-axis oriented along the thickness direction. Symmetry allows for consideration of only a half-layer. The governing equation for reactive diffusion is[21]

$$D_{PA}\frac{\partial^2 w}{\partial z^2} - k_{PA}w = \frac{\partial w}{\partial t}\left(0 \leq z \leq \frac{h_{PA}}{2}\right),\qquad(1)$$

where D_{PA} is the water diffusivity in the polyanhydride layer, k_{PA} is the reaction rate constant between water and the PA, and w is the water concentration which depends on both location z and time t. The boundary conditions at $z = 0$ and $z = \frac{h_{PA}}{2}$ are zero water flux and constant water concentration, $w_0 = 1$ g cm^{-3}, corresponding to $\frac{\partial w}{\partial z}\Big|_{z=0} = 0$ and $w|_{z=\frac{h_{PA}}{2}} = w_0$, respectively. The initial state involves zero water concentration throughout the PA, or $w|_{t=0} = 0$ $(0 \leq z < \frac{h_{PA}}{2})$. The method of separation of variables yields an analytic solution for w (see details in Experimental Section). The thickness of the dissolved PA in the half-layer can be obtained by integration of $\frac{h_{PA}M_{PA}k_{PA}w}{2q\rho_{PA}M_{H_2O}}$ over both z and t, where M_{PA} (=481.48 g mol^{-1} for PA-90 and 638.4 g mol^{-1} for PA-70) and M_{H_2O} (=18 g mol^{-1}) are the molar masses of the PA and water, respectively, ρ_{PA} (=1.293 g cm^{-3} for PA-90 and PA-70) is the mass density of the PA, and q_{PA} (=1) the number of water molecules reacting with each molecule of the PA (here the molar mass of the repeating unit with one anhydride group in the crosslinked polyanhydrides is used to simplify the calculation and correspondingly the reaction with water is also assumed to be with one anhydride group). The remaining thickness, h, of the entire PA layer during degradation is as below:

$$\begin{aligned}h = h_{PA} - \frac{2w_0 M_{PA}\sqrt{k_{PA}D_{PA}}}{q_{PA}\rho_{PA}M_{H_2O}}&\left\{\tanh\sqrt{\frac{k_{PA}h_{PA}^2}{4D_{PA}}}t - 4h_{PA}^3\sqrt{k_{PA}D_{PA}}\right.\\ &\left.\times \sum_{n=1}^{\infty}\frac{1}{\left[k_{PA}h_{PA}^2 + D_{PA}\pi^2(2n-1)^2\right]^2}\left\{1 - \exp\left\{-\left[k_{PA} + \frac{4D_{PA}\pi^2(2n-1)^2}{h_{PA}^2}\right]t\right\}\right\}\right\}\end{aligned}\qquad(2)$$

From experimentally measured changes in the thicknesses of films of PA in PBS solution (37 °C) with two different initial thicknesses, the water diffusivity, D_{PA}, and reaction rate constant, k_{PA}, can be determined by Equation 2. Figure S7b represents theoretical (lines) and

measured (dots) changes in thickness of PA-90 and PA-70 with different initial thicknesses. Here, D_{PA} and k_{PA} are 1.2×10^{-14} m^2 s^{-1} and 5×10^{-7} s^{-1} for PA-90, and 7×10^{-15} m^2 s^{-1} and 3.5×10^{-7} s^{-1} for PA-70.

In Figure 2c and Figure S7c, a bilayer model can provide a way to examine biofluid barrier properties of different PA films, where the initial thickness of the underlying Mg layer is h_{Mg}. Both layers follow governing equations of reactive diffusion similar to that of the single layer model, i.e.,

$$D_{Mg}\frac{\partial^2 w}{\partial z^2} - k_{Mg}w = \frac{\partial w}{\partial t}\left(0 \leq z \leq h_{Mg}\right) \tag{3}$$

for Mg, and

$$D_{PA}\frac{\partial^2 w}{\partial z^2} - k_{PA}w = \frac{\partial w}{\partial t}\left(h_{Mg} \leq z \leq h_{Mg} + h_{PA}\right) \tag{4}$$

for the PA. Here, D_{Mg} is the water diffusivity in Mg and k_{Mg} is the reaction rate constant between water and Mg. Besides the initial condition $w|_{t=0} = 0$ and the boundary conditions $\frac{\partial w}{\partial z}\big|_{z=0} = 0$ and $w|_{z=h_{Mg}+h_{PA}} = w_0$, continuity of water concentration and water flux across the Mg/PA interface requires $w|_{z=h_{Mg}-0} = w|_{z=h_{Mg}+0}$ and $D_{Mg}\frac{\partial w}{\partial z}\big|_{z=h_{Mg}-0} = D_{PA}\frac{\partial w}{\partial z}\big|_{z=h_{Mg}+0}$. The method of separation of variables yields an analytic solution for the water concentration (see details in Experimental Section). As with the single layer model, the results yield expressions for the remaining thickness of the Mg layer, h', which in turn gives the electrical resistance of the Mg layer, R, by $R = R_0\frac{h_{Mg}}{h'}$, where R_0 is the initial resistance. Omitting the contribution of a series summation that is negligible in this study yields the following,

$$R \approx \frac{R_0}{1 - \frac{w_0 M_{Mg}t}{q_{Mg}\rho_{Mg}M_{H_2O}h_{Mg}} \times \frac{\sqrt{k_{Mg}D_{Mg}}csch\sqrt{\frac{k_{PA}h_{PA}^2}{D_{PA}}}}{\sqrt{\frac{k_{Mg}D_{Mg}}{k_{PA}D_{PA}}} + coth\sqrt{\frac{k_{Mg}h_{Mg}^2}{D_{Mg}}}coth\sqrt{\frac{k_{PA}h_{PA}^2}{D_{PA}}}}} \tag{5}$$

Figure 2d shows the change in resistance of a 300 nm thick layer of Mg encapsulated by different layers of PA as a function of immersion time in PBS solution (37 °C). The theoretical (lines) and measured (dots) results agree very well. Here, $k_{Mg} = 9 \times 10^{-3}$ s^{-1}, $D_{Mg} = 1.2 \times 10^{-15}$ m^2 s^{-1},[17] $\rho_{Mg} = 1.738$ g cm^{-3}, $M_{Mg} = 24$ g mol^{-1}, and $q_{Mg} = 2$ according to $Mg + 2H_2O \rightarrow Mg(OH)_2 + H_2$. Considering PA-70/90 as an equivalent layer with D_{PA} and k_{PA} of 1.1×10^{-14} m^2 s^{-1} and 4×10^{-7} s^{-1}, respectively, produces results that fall reasonably between those of PA-70 and PA-90. Figure S7d shows the change in resistance of a 20 μm thick layer of Mg encapsulated by different PA layers using measured and theoretical results based on the parameters for 300 nm thick Mg. Up to 3 h after

immersion, the theoretical and measured results agree well. For 6 h and thereafter, the measured resistance increases faster than modeling results, consistent with an accelerated rate of dissolution of Mg, as expected by the degradation of PA in Figure 2a and Figure S7b. At short times (<3 h), the extent of degradation of PA is minimal, such that dissolution of Mg results only from the penetration of water through the PA. At long times (>6 h), degradation of the PA becomes significant, such that the acidic byproducts accelerate the dissolution of Mg.

Studies of the degradation of RF receiver coils encapsulated by PA-90 and PA-70 involves embedding them in 2% agarose gel at 37 °C, as a mimic of the subcutaneous tissue environment (Figure 2e). The coils completely disappear by hydrolysis to $Mg(OH)_2$ in 3 days, while the degradation products remain inside the soft capsule of PA-70 structure. As water permeates through the outer PA-70 layer (Figure S7–8), degradation of the inner PA-90 structure and accelerated dissolution of Mg commences. Previous investigations by Fourier transform infrared spectroscopy show that the characteristic stretching vibration peak from the anhydride group decreases and a peak associated with carboxylic acid appears during hydrolysis.[18a, 18b] These findings provide further evidence that hydrolysis of the PA generates carboxylic acid, as mentioned previously. The acidic environment accelerates the dissolution of Mg via $2H^+ + Mg \rightarrow Mg^{2+} + H_2$.

In addition to the chemical properties, the mechanical characteristics are also important to avoid mechanically induced damage of muscle and skin during motions (Young's modulus, E: 10 KPa- 10MPa).[22] Figure S9a and b show stress-strain curves for PA-90 and PA-70; the results indicated an elongation at break of 31.2% and 38.4%, respectively, and Young's moduli 2.83 ± 0.21 MPa and 3.44 ± 0.05 MPa, respectively. The elastic properties represent advantages in tissue biocompatibility compared to PLGA (E: 2.5 GPa) used in previous report[14] and other alternative bioresorbable polymers such as poly (lactic-acid) (E: 2.5 GPa) and polycaprolactone (E: 400 MPa).[23]

Figure 2f summarizes results of in vivo characterization of degradation of the device encapsulated by PA-90 and PA-70. The images show that the encapsulated receiver coils disappear completely, with only a small amount of polymer residue after 3 days. All solid material disappears within 10 days. In vivo studies using mouse models examine this bilayer PA encapsulated stimulator along with an otherwise similar device encapsulated with PLGA via CT imaging (Figure S10; 800 nm-thick coating of tungsten improves the contrast in the images; this material remains after the Mg coil disappears). For the PA encapsulated stimulator, the shape of the coil becomes unrecognizable after one day, while for the PLGA encapsulated device, the coil remains visible after two weeks.

2.3. In vitro and in vivo studies of biocompatibility

In vitro evaluations of the biocompatibility of the components and the PAs precede their use in animal models. Previous studies show that the Mg, PLGA, Si and sodium alginate are biocompatible.[14] The work reported here focuses, therefore, on different formulations of PAs as coatings on well plates for cell-based assays with C2C12 myoblasts and spinal motor neurons (Figure S11). All conditions involve tests in triplicate.

Fluorescence imaging of cells stained with Hoechst (Blue: total cells), PI (Red: dead cells), and Calcein AM (Green: live cells) after 24 h in culture show that formulations of PA with high ratios of 4-PA (PA-90) cause cell death (Figure S11a and b), consistent with their rapid degradation and subsequent decrease in pH. In C2C12 myoblast cultures, increases in the numbers of PI-positive dead cells and decreases in the number of Hoechst-positive total cells indicate decreased cell attachment and increased death among the remaining attached cells in PA-80 (cell viability: 60.5%) and PA-90 wells (cell viability: 32.8%) compared to controls. Motor neurons show less sensitivity to PA byproducts, with no statistical differences in ratio of PI-positive dead cells by treatment group (Figure S11d). Similar tests using PA mixtures with lower ratios of 4-PA (PA-70, PA-60, and PA-50) show no reduction in cell viability for either cell type tested, with results that are equivalent to control cells cultured under standard conditions (C2C12 cell viability: 98.7%, 99.9%, and 99.6%).

Measurements of lactate dehydrogenase (LDH) levels in media samples retrieved 3- and 24-hours after C2C12 cell seeding provide additional insights. LDH levels at 3 h (Figure S11c) follow the same pattern as live-cell fluorescent staining results, with significantly elevated LDH levels for PA-80 and PA-90 (control: 0.169 ± 0.014, PA-80: 1.451 ± 0.148, PA-90; 1.111 ± 0.132) and with no differences compared to controls for lower ratios of 4-PA (PA-70: 0.150 ± 0.010, PA-60: 0.138 ± 0.018, PA-50: 0.138 ± 0.018). The disparities in LDH concentration between different ratios of 4-PA are smaller and non-significant in the LDH samples taken 24 h post-seeding (Figure S11c), probably due to cell death at early stage. LDH levels at 3- and 24- hours after motor neuron cell seeding demonstrates no significant difference between different groups, which also indicates motor neurons are less sensitive to PA and its byproducts (Figure S11e).

Additional studies highlight the key acidity regulation features through examination of two samples at 37 °C, with one sample of bilayer design where PA-90 (thickness: ~180 μm) places within a soft capsule of PA-70 (thickness: ~20 μm) in 3 mL PBS solution, and the second with single layers of PA-70 (20 μm) and PA-90 (180 μm) both immersed directly in 3 mL PBS solution (Figure S12a); the pH values of the surrounding solution are 6.5 ± 0.1 and 5.4 ± 0.1 respectively after 24 h (Figure S12b). The pH for the bilayer sample is approximately equivalent to the pH of PA-70 in the degradation test in Figure 2b, indicating that there is negligible leakage of acidic products of PA-90, and in the full device, the acidic product from PA-90 degradation mainly reacts with Mg. Additional studies of the bilayer structure with a colorimetric pH indicator embedded between PA-90 layer in Figure S12c–d also proves the effectiveness of PA-70 soft capsule without leakage of PA-90, yielding a pH of ~5 inside the soft capsule after 24 h.

In vivo evaluations of the biocompatibility of PA-70 in a mouse model in Figure 3a demonstrate that changes in mouse body weight with PA-70 are similar to those with control implants (PLGA) during the four-week period of study. The changes in weight of major organs (heart, lung, liver, kidney, spleen, and brain) explanted from mice two- and four- weeks post implantation in Figure 3b show minimal differences, indicating no gross damage to the organs. In Figure 3c, d and Figure S13, during the four weeks period, the complete blood counts and blood chemistry tests show no significant change, indicating absence of organ injury or damage, and no change in the enzyme and

electrolyte balance. The average counts of white blood cells, red blood cells, hemoglobin, hematocrit, mean corpuscular volume, mean corpuscular hemoglobin, and platelets, all indicate no signs of any abnormalities, including anemia, bleeding disorder, heart attack, liver disease, and nutritional deficiency. (Figure 3c and Figure S13a). Blood chemistry results are also comparable to control values (Figure 3d and Figure S13b), indicating normal enzyme and electrolyte levels, therefore showing no signs of metabolic disorders or organ-specific diseases. Specifically, normal levels of albumin, alanine aminotransferase, alkaline phosphatase, aspartate transaminase and total protein suggest normal liver function. Normal levels of creatinine and blood urea nitrogen indicate normal kidney function. Normal levels of calcium, sodium, potassium, chloride, phosphorus, and glucose indicate normal function of the metabolic system. In Figure S14–15, histological analysis of major organs, brain, heart, lung, liver, kidney, and spleen, demonstrate no identifiable increase in immune cells caused by implantation of PA-70. Thus, the inflammation in skin tissue from implantation sites in both the PLGA control group and the PA-70 group is due to surgical implantation procedures generally, rather than due to the material constituents of the implants.

After confirming the biocompatibility of PA-70, we implanted another set of mice with the complete device to evaluate in-vivo biocompatibility of the bilayer design to compare with control group undergoing shame surgery. No skin or muscle abnormalities are detected at 3 or 10 days, compared to skin and muscle tissue from control animals undergoing sham surgery with no implant. The bilayer strategy successfully minimizes inflammation and damage of tissue surrounding the implanted device. Hematoxylin and Eosin (H&E) stained sections of the back subdermal skin and muscle tissue surrounding the implanted site demonstrate no development of fibrosis, heightened immune reaction, or inflammation when examined 3 days or 10 days post-implantation (Figure 3e). All implanted devices contain a bilayer of PA-90 and PA-70, with the same geometry specified in Figure 1a unless noted.

2.4. In vivo tests of the electrical performance of the wireless bioresorbable stimulator

Evaluations in the context of regeneration of the sciatic nerve in a mouse model of tibial nerve transection begin with surgical exposure of the nerve at the mid-thigh level and implantation of the wireless or the wired stimulator, as shown in Figure 4a and Figure S16. Insertion of the receiver coil subcutaneously aligns the PLGA cuff and Mg electrode with the nerve. Wrapping the Mg electrode and PLGA cuff around the nerve establishes the electrical interface for stimulation, while minimizing electrical leakage to the surrounding biofluid. Suturing the incision completes the surgery and enables wireless ES with an external antenna. Implantation of the wired stimulator follows similar steps but with external wires connected directly to the implanted electrical leads rather than a wireless external antenna as the source of power, as shown in Figure S16.

c-Fos staining in Figure S17 clearly demonstrates recent neuronal activity in DRG neurons induced by ES treatment in both wired and wireless animals, but not sham, when animals are sacrificed one-hour post-treatment. Monitoring evoked compound muscle action potentials (CMAPs) during ES establishes that the wireless stimulator achieves relevant levels of ES, with 87.9%±17.4% of the wired response magnitude (n=22 mice; $R^2 = 0.7585$, Figure 4b, c). Recording of CMAPs occurs midway along the right tibialis anterior muscle (TA) using

a 30-gauge concentric needle electrode. The experiments involve increasing the stimulation voltage until the CMAP magnitude plateaus at the physiological maximum. Because the TA is innervated by the fibular nerve, which is a distal branch of the sciatic nerve that is left intact in our tibial nerve transection model, recording from TA yields an unimpaired neuromuscular response that enables continuous monitoring of ES treatment.

Measurements of CMAPs before and after one-hour of wireless stimulation determined that power delivery is sufficient to fully activate neurons with axons projecting to the injured nerve for the full duration of stimulation, with no loss of power over the course of the ES session (Figure 4d). Muscle twitching is an additional indicator of stimulation that complements electrophysiological recordings to verify stimulation levels and consistency in operation (Video S1).

In addition, comparing pre-surgical fibular nerve conduction by CMAPs and sensory nerve action potentials (SNAPs) (SNAPs data measured from the 2nd toe of the right hind paw yield unimpaired sensory nerve information from the fibular nerve) recordings against identical recordings measured either 3 days or 10 days later showed no negative impact on maximal response magnitude in uninjured animals, showing that the PLGA nerve cuff does not compress or otherwise harm the nerve's ability to function (Figure S18 and Table S2).

2.5.   Spinal Motor Neuron Retrograde Tracing and Tibial Nerve Regeneration

Evaluations of tibial nerve reinnervation focus on the number of reinnervating motor neurons observed in the spinal cord after retrograde labeling, and the growth of axons distal to the injury site, as summarized in Figure 5. Fluorescent retrograde tracer applied 3mm distal to the site of tibial nerve repair, produces robustly labeled fluorescent motor neuron somas in the spinal cord. Comparisons of the numbers of retrogradely labeled motor neurons in spinal cord sections (Figure 5a) indicate that ES significantly enhanced regeneration compared to sham (Fisher's LSD test $p=0.0227$; Figure 5b–d). Furthermore, the results indicate no significant difference between motor reinnervation in the wired and wireless groups (Student t-test $p=0.2474$; Figure 5c).

After the nerve injury, the distal axons undergo Wallerian degeneration and leave behind an endoneurial tube devoid of axons. Measuring the amount of reinnervation by axons beyond the site of the injury (Figure 5e) serves as a means to study the extent of axonal sprouting and regeneration. Compared with the sham group, both wired and wireless groups show an enhanced level of axon reinnervation, consistent with facilitation of axonal regeneration capacity (one-way ANOVA, $p=0.0281$; Figure 5f).

2.6.   CMAP Recovery

Post-transection, maximum CMAP amplitudes recorded from TA muscle acutely diminish and then gradually recover as axons regenerate. Analyses of the maximum negative peak amplitude (a standard clinically relevant CMAP component) recorded 21 days post-injury, show treatment-dependent recovery trajectories when normalized to pre-injured baseline (one-way ANOVA $p=0.0260$). The wire and wireless groups show significantly enhanced CMAP recovery compared to sham (Fisher's LSD test $p=0.0295$ and $p=0.0114$, respectively;

Figure 5g), but do not differ significantly from each other. Furthermore, the wire and wireless groups show significantly less prolonged CMAP latency compared to sham (Fisher's LSD test p=0.0037 and p=0.0003, respectively; Figure 5h), but do not differ significantly from each other. In agreement with comparable studies on ES, significant treatment effects on histologic and electrophysiologic outcomes (Figure 5g–h) arise earlier than changes in sensorimotor behavioral assessments,[24] which is why they were selected as the principle outcomes of this study. Weekly grip strength measurements were made up to 3 weeks post-repair, but neither the ES groups nor sham showed any behavioral recovery within this timeframe (Figure S19).

3. Conclusion

A bilayer encapsulating structure formed with tailored formulations of PA serves as the basis for a bioresorbable, wireless platform optimized to deliver one-hour, post-operative ES to enhance rates of recovery from peripheral nerve injury, with fast rates of bioresorption after this critical time period. This fast mode of resorption minimizes risks associated with unnecessary device load following stimulation. The results complement those associated with previously reported, long-lived bioresorbable devices that enable extended periods of stimulation, as a direct replacement for current clinical practice that involves stimulation in the intraoperative period. The strategy introduced here accelerates the processes of device resorption and contains fragments that result from these processes, to eliminate most of the devices within 3 days and complete resorption within 10 days. These materials and device concepts have potential for broad utility across applications in bioresorbable electronics with short operational lifetime requirements.

The motor neuron count and distal nerve section results of one-hour ES with these systems in mouse tibial nerve transection model with this wireless bioresorbable stimulator confirm that early-stage peripheral axon regeneration is accelerated in ES group compared with control group, and the wireless stimulator can achieve similar regeneration effect as wired electrodes.

The limitations of the current platform and previously reported long-lived variants are that the lifetimes depend on the available materials choices and structure geometries. Recent advances in stimuli-responsive materials, such as optically/thermally responsive polymers, have potential for devices that degrade rapidly after a user-defined triggering event.[25] The integration of sensor functionality presents another set of opportunities, allowing for closed loop control of both operating parameters and device lifetime.

4. Experimental Section

Fabrication of the fast-bioresorbable wireless electrical stimulator:

The fabrication began with preparation of each component separately, followed by assembly into a complete wireless stimulator for test and qualification. Chemical etching of a Mg foil (100 μm thick, 99.99% grade) in a mixture of acetic acid and deionized water (50:1) yielded foils with desired thicknesses (~10 μm for the coil and ~40 μm for the electrodes). Cutting the foil into small pieces (~12 mm x12 mm) and laminating onto

a poly(dimethylsiloxane) (PDMS, 10:1) stamp allowed transfer to the PA-90 substrate. Synthesis of the polyanhydride (take PA-90 as an example) involved mixing the monomers, 4-PA (9 mmol, 1.640 g), PEG diacrylate (1 mmol, 0.25 g), PETMP (5 mmol, 2.444 g), and 2,2-dimethoxy-2-phenylacetophenone (photoinitiator, 0.1% of total mass), each obtained from Sigma-Aldrich (MilliporeSigma) and used as received, in a 20-mL vial via magnetic stirring and vortex mixing until complete dissolution. Drop-casting the mixture on the foil or the assembled device and subsequently cured by exposure to UV light (Cole-Parmer model 9762000, 4 Watt, 365 nm) for 15 min. After curing, the Mg/PA was peeled from the PDMS substrate and flipped. An UV laser cutter (LPKF, ProtoLaser U4) defined the coil structure by selectively removing Mg from the PA substrate. A film of sodium alginate (~20 μm thick, Scientific Inc) bonded two such coils and served as a dielectric spacing layer in between. Fabrication of the Si NM diode followed procedures described elsewhere.[14] Laser cutting the Mg foil (~40 μm) defined electrodes (width: ~340 μm) with inter-electrode distances of ~2 mm and interconnect traces with lengths of 3 mm, embedded between two layers of PLGA (~20 μm thick) by hot-pressing. A conductive wax electrically connected all of the components of the device.[26] Applying an encapsulation of PA-70 (~20 μm thick) onto the receiver coil and electrical interconnections completed the fabrication.

Experimental setup for the wireless and wired stimulator:

For the wireless stimulation, a waveform/function generator (Rigol DG1032Z) (voltage: 100–700 mVpp) and amplifier (Electronics & Innovation, 201L) provided electrical power to an external antenna (3 turns of wire, diameter: ~4 cm) placed above the animal to ensure good electromagnetic coupling with the implanted receiver coil.

The wired stimulation was powered by a Grass stimulator (Model SD9B) connected to implanted electrode leads made with Mg wires and PLGA cuff as mentioned in the fabrication section above.

Functional lifetime of the wireless electrical stimulator:

Testing of the functional lifetime involved an LED electrically connected to the wireless stimulator as a visual indicator. Soaking in PBS (pH=7.4) at 37 °C demonstrated stable operation for up to 5 h (Figure S1). In Figure S2, the setup measured the electrical stability of the wireless stimulator in a in vivo mimicking condition quantitatively. The input voltage from the waveform generator (Agilent 33250A) remained constant at $V_{PP} = 20$ V. The oscilloscope (Tektronix TBS 1032B) measured the output voltage from the wireless stimulator and the network analyzer (Keysight, N9923A) recorded the RF properties. After measurement, the wireless stimulator was immersed in 0.6% agarose gel in vivo mimicking condition at 37 °C. The RF properties and output voltage from the wireless stimulator operated stably with slight drift during the first 5 hours and failed to deliver enough electrical stimulation after 7 hours. In vivo studies indicated a maximum CMAP evoked by wireless stimulation, unchanged during stimulation for 1 h.

RF characterization including the effects of the surrounding biofluid:

Characterization of the RF properties (Figure S3) and the output voltage (Table S1) relied on a network analyzer (Keysight, N9923A) for measurements at various conditions, including

cases of the wireless stimulator with no PBS, with PBS only on the coil, with PBS on the exposed electrodes, and with PBS on both the coil and electrodes. The output voltage from the exposed electrode was measured with an oscilloscope where the power was from the waveform generator (voltage: 10 Vpp). The measurements indicted a significant effect of the PBS on the RF behavior and output voltage. Use of an extended PLGA cuff to prevent entry of fluids into this region of the system enhanced the stability of the electrical interface and the overall performance.

Electromagnetic simulation of the RF behavior:

Finite element analysis of the electromagnetic characteristics allowed study of the influence of the thickness of the receiving coil in inductive coupling. Here, the change of the scattering parameter S11 (in dB) of transmitting coil described the coupling for the different trace thickness: where the most negative value of S11 corresponds to the tighter coupling (Figure 1d and Figure S5) The simulations used the commercial software ANSYS HFSS, in which tetrahedron elements were used in the solution with adaptive meshing convergence. An adaptive convergence condition and a spherical radiation boundary (radius of 1000 mm) were adopted to ensure computational accuracy. The simulation used the default material properties included in the HFSS material library.

Degradation test of the polyanhydride film:

Preparation of the mixture of PA precursors used procedures described previously. Pouring the mixture into a PDMS mold (2 cm × 1 cm × 50 μm) and then photopolymerizing the system by UV irradiation for 15 min yielded a solid film. After weighing, the PA was immersed into 50 mL PBS at 37 °C. The film was then removed from the PBS, dried, weighed, and returned to a new bath of PBS every 12 h. For studies of the changes in, associated with dissolution of the PA, the polymer concentration was maintained at 1 mg/mL and a pocket ion sensitive field transistor pH meter (DeltaTrak, Model 24004) measured the pH of the solution every 12 h without renewal of the PBS solution. Each measurement was repeated for three individual samples at each composition.

Water permeation tests of polyanhydride film:

A water-soluble green dye (Wilton, concentrated ice gel paste) allowed direct visualization of the permeation of water through films of PA-70. First, the dye was placed onto a glass slide, then the film of PA-70 was formed on top of the dye by filling PA-70 into PDMS molds with different thicknesses following by UV irradiation. A marine epoxy (Loctite) further sealed the edges of the films. The time of dye diffusion was monitored during immersion in PBS at 37 °C. The time for the area of the dye to spread to areas of roughly twice the initial area defined a threshold for permeation of water through the film.

Water permeability test with Mg resistor:

To further quantify water permeation through the film and reaction with underlying Mg traces, the resistance of Mg served as an indicator of water permeation and generation of acidic products during the degradation of the PA. Electron-beam evaporation and photolithography formed patterned films of Mg resistors with thicknesses of 300 nm. Laser

cutting of Mg foils yielded structures of Mg resistors with 20 μm thickness. Applying layers of PA on these Mg resistors and introducing PBS into a PDMS well structure with edges sealed by marine epoxy defined a simple setup for measuring the water permeation and the changes in resistance.

Analytic solution of water concentration by the reactive diffusion model:

By applying the method of separation of variables to the equation of reactive diffusion for the single layer model of polyanhydride, incorporating both the boundary and initial conditions, the analytic expression for water concentration distributed in the polyanhydride was

$$
w = w_0 \left\{ \frac{\cosh\left(\sqrt{\frac{k_{PA}}{D_{PA}}} Z\right)}{\cosh\left(\sqrt{\frac{k_{PA} h_{PA}^2}{4 D_{PA}}}\right)} + \sum_{n=1}^{\infty} \frac{4(-1)^n (2n-1)\pi}{\frac{k_{PA} h_{PA}^2}{D_{PA}} + [(2n-1)\pi]^2} \right.
$$
$$
\left. \times \exp\left\{ -\left\{ k_{PA} + D_{PA}\left[\frac{(2n-1)\pi}{h_{PA}}\right]^2 \right\} t \right\} \cos\left[\frac{(2n-1)\pi z}{h_{PA}}\right] \right\}
\tag{6}
$$

for $0 \le z \le \frac{h_{PA}}{2}$. The water concentration distribution for $-\frac{h_{PA}}{2} \le z \le 0$ followed from the symmetry with respect to $z = 0$.

By applying the method of separation of variables to the equations of reactive diffusion for both the PA and the underlying Mg, incorporating the boundary, continuity, and initial conditions, the water concentration distributed in the Mg/PA bilayer was

$$
w = w_0 \left[\sum_{n=1}^{\infty} C_n \exp(-\lambda_n t) f_n(z) + g(z) \right]
\tag{7}
$$

where

$$
f_n(z) = \begin{cases} \sin\left(\sqrt{\frac{\lambda_n - k_{PA}}{D_{PA}}} h_{PA}\right) \cos\left(\sqrt{\frac{\lambda_n - k_{Mg}}{D_{Mg}}} z\right), & 0 \le z \le h_{Mg} \\ \cos\left(\sqrt{\frac{\lambda_n - k_{Mg}}{D_{Mg}}} h_{Mg}\right) \sin\left[\sqrt{\frac{\lambda_n - k_{PA}}{D_{PA}}} (h_{Mg} + h_{PA} - z)\right], & h_{Mg} \le z \le h_{Mg} + h_{PA} \end{cases}
\tag{8}
$$

and

$$
g(z) = \begin{cases} F \cosh\left(\sqrt{\frac{k_{Mg}}{D_{Mg}}} z\right), & 0 \le z \le h_{Mg} \\ \cosh\left(\sqrt{\frac{k_{PA} h_{PA}^2}{D_{PA}}} \frac{h_{Mg} + h_{PA} - z}{h_{PA}}\right) - G \sinh\left(\sqrt{\frac{k_{PA} h_{PA}^2}{D_{PA}}} \frac{h_{Mg} + h_{PA} - z}{h_{PA}}\right), & h_{Mg} \le z \le h_{Mg} + h_{PA} \end{cases}
\tag{9}
$$

with

$$F$$

$$= \frac{1}{cosh\sqrt{\frac{k_{Mg}h_{Mg}^2}{D_{Mg}}}cosh\sqrt{\frac{k_{PA}h_{PA}^2}{D_{PA}}} + \sqrt{\frac{k_{Mg}D_{Mg}}{k_{PA}D_{PA}}}sinh\sqrt{\frac{k_{Mg}h_{Mg}^2}{D_{Mg}}}sinh\sqrt{\frac{k_{PA}h_{PA}^2}{D_{PA}}}} \qquad G = \frac{tanh\sqrt{\frac{k_{PA}h_{PA}^2}{D_{PA}}} + \sqrt{\frac{k_{Mg}D_{Mg}}{k_{PA}D_{PA}}}tanh\sqrt{\frac{k_{Mg}h_{Mg}^2}{D_{Mg}}}}{1 + \sqrt{\frac{k_{Mg}D_{Mg}}{k_{PA}D_{PA}}}tanh\sqrt{\frac{k_{Mg}h_{Mg}^2}{D_{Mg}}}tanh\sqrt{\frac{k_{PA}h_{PA}^2}{D_{PA}}}}. \qquad (10)$$

λ_n ($n = 1,2,3,\cdots$) were determined by the transcendental equation

$$tan\sqrt{\frac{(\lambda - k_{Mg})h_{Mg}^2}{D_{Mg}}}tan\sqrt{\frac{(\lambda - k_{PA})h_{PA}^2}{D_{PA}}} = \sqrt{\frac{(\lambda - k_{PA})D_{PA}}{[(\lambda - k_{Mg})D_{Mg}]}}, \text{ and } C_n = -\frac{\int_0^{h_{Mg} + h_{PA}} f_n(z)g(z)dy}{\int_0^{h_{Mg} + h_{PA}} f_n^2(z)dy}.$$

In vitro and in vivo degradation tests of wireless electrical stimulators:

Testing used a 2% agarose gel, formed by dissolving 2% wt agarose in PBS by heating the solution to boil and stirring for 1 min then cooling down, as a simple mimic for muscle and skin tissue to examine degradation of the wireless stimulator in vitro. The experiments involved placing the wireless stimulator between two pieces of this gel at 37 °C. Photographs captured the coils degradation daily until the Mg coils completely disappeared at the third day. In vivo degradation tests involved implanting the wireless stimulator subcutaneously in the back region of a mouse model. Photographs captured the in vivo degradation of the wireless stimulator 3 days and 10 days after implantation.

Leakage test of bilayer encapsulation strategy:

Tests of bilayer PA-70 (thickness: 20 μm, diameter: 10 mm) & PA-90 (thickness: 170–180 μm, diameter: 8 mm) encapsulation structures included comparisons of pH value to those associated with both single layers of PA-70 (20 μm) and PA-90 (170–180 μm) together in one container. A schematic illustration of the setup appears in Figure S12a. A colorimetric universal pH indicator embedded in the encapsulation structure allowed visualization of variations in pH through changes in color. Similar approaches provided methods for evaluation of leakage of acidic species into the surrounding PBS. Specifically, a universal indicator (RICCA) was drop cast onto the first PA-90 layer (170–180 μm), before forming the layers of PA-70 (20 μm) and the second layer of PA-90. A pH meter provided measurements of the pH of the surrounding solution as a function of time after immersion in 3 mL PBS (initial pH: 7.2) at 37 °C. The test sample was immersed in 3 mL PBS (initial pH: 7.2) at 37 °C and imaged every 12 h. Colorimetric references consisted of samples of indicator immersed in citrate-phosphate buffer solution with pH between 2 (red) and 7 (green).

Cell culture:

Tests of biocompatibility used C2C12 immortalized mouse myoblasts (ATCC, Manassas, VA) and iPSC-derived human motor neurons cultured separately in 24-well plates. The plates were coated by adding the precursor mixture for polyanhydride and photopolymerizing under UV irradiation for 15 minutes. Additional irradiation (3 hours on each side, top and bottom) sterilized the polyanhydride. For C2C12s, a coating of sterile 5% porcine gelatin was applied (G1890, Millipore-Sigma, Burlington, MA). C2C12 cells passaged and counted immediately prior to seeding formed a population density of

2.0×10^4 cells/well, and cultures were fed with Dulbecco's Modified Eagle Medium (15017CV, Corning Inc., Corning, NY) plus 10% fetal bovine serum by volume. As previously described, motor neurons were differentiated and cultured on plates coated with Poly-D-Lysine (P6407–5MG, Sigma-Aldrich) and laminin (23017–015, Thermo Fisher) at a seeding density of 3.0×10^4 cells/well.[27] MNs were fed with complete neurobasal media (95% Neurobasal Media, Life Tech 21103–049; 1% Non-Essential Amino Acids, Corning 25025111; 1% Glutamax, Life Tech 35050–061; 1% N2, Life Tech 17502–048; 2% B27, Life Tech 17504–044) supplemented with 0.1% Ascorbic Acid (Sigma-Aldrich A4403), 0.01% BDNF (R&D 248-BD), 0.01% CNTF (R&D 257NT/CF), 0.01% GDNF (R&D 212-GD), and 0.1% ROCK Inhibitor (Tocris 1254) by volume.

Cell viability assays:

Lactate dehydrogenase (LDH) is an enzyme released upon cell breakdown, and therefore an aggregate measure of cell death. Measurements of LDH levels in samples of cell media used a commercially available colorimetric assay (CytoTox 96® Non-Radioactive Cytotoxicity Assay, Promega, Madison, WI). Identical culture media from wells without cells assayed alongside the experimental groups served as a control.

Live-cell imaging occurred after 24 hours in culture, with fluorescent cell markers to identify cell survival status. Calcein AM (Thermo Fisher Scientific, Waltham, MA) labeled living cells, permeating the intact cell membrane and undergoing conversion to its fluorescent form via intracellular esterase activity. Propidium Iodide (Thermo Fisher Scientific), which is membrane impermeant, labeled dead cells with degraded cell membranes. Hoechst (Thermo Fisher Scientific) labeled DNA in all cells regardless of cell survival status. 20x images were obtained from the center of each well using an inverted microscope (Leica Dmi8-S Inverted Microscope System), followed by blinded quantification of cell survival in ImageJ.[28]

In Vivo Evaluation of Biocompatibility:

Female CD1 mice (7 weeks old) were purchased from Charles River Laboratories (Wilmington, MA). All animal handling and experimental protocols were approved by the Institutional Animal Care and Use Committee at Northwestern University. Mice were housed four per cage and maintained on a 12:12 light: dark cycle (lights on at 6 AM); and given ad libitum access to food and water throughout the study. On surgery day, mice were anesthetized with isoflurane gas (≈2%), then overnight UV exposure sterilized samples of PLGA (control, $4 \times 4 \times 0.02$ mm) and PA-70 ($4 \times 4 \times 0.2$ mm) were implanted in the dorsal interscapular region within a 0.5- to 1-cm-length subcutaneous pocket. The incisions were closed using 5.0 monofilament absorbable surgical sutures. Following the surgery, mice were monitored daily for general condition and behavior, and body weights were measured twice weekly. At 2 weeks and 4 weeks post implantation, mice (3 mice per each time point) were euthanized for histology and blood analysis. Major organ, including brain, heart, kidneys, liver, lung, spleen, and the skin immediately adjacent to the implant were collected, weighed (except skin) and placed in fixative. The explanted organs were stored in 10% buffered formalin (1:10 volume ratio) in 50-ml conical tubes to prepare the tissue samples for histology studies. Tissue samples were embedded in paraffin, sectioned and

stained with H&E for histological analysis. Blood samples were also collected via cardiac puncture and split into K_2-EDTA tubes and additive-free tubes. Complete blood counts and blood chemistry tests were conducted at Veterinary Diagnostic Laboratory at University of Illinois. Lymphocytes were identified by morphology from ten distinct regions by $400 \times$ fields per sample.

Experimental mice group design:

Mice were randomized to one of three treatment groups using www.Random.org 's online list randomization,[29] maintaining sex balance between groups. All groups received identical tibial nerve injuries and repairs. The wired ES group received tibial nerve transection injury with direct anastomosis and wired stimulator implant, with 1 hour of ES immediately post-repair. The wireless ES group received tibial nerve transection injury with direct anastomosis and wireless stimulator implant, with 1 hour of ES immediately post-repair. The control group received tibial nerve transection injury with direct anastomosis and device implant, but no ES. All mice remained under anesthesia for 1-hour post-surgery.

Animal care:

All animal use procedures were approved by Northwestern University's Institutional Animal Care and Use Committee and performed in full compliance with the National Institutes of Health Guide for the Care and Use of Laboratory Animals and the guidelines of the National Society for Medical Research. All mice in the study were young adult C57Bl/6J mice weighing between 25–35 g, with equal numbers of males and females housed in same-sex groups of three littermates (The Jackson Laboratory, Bar Harbor, ME). Mice were housed in Northwestern University's animal care facilities on a 12/12 h light cycle, with mouse chow and water available ad libitum. Pain and distress were monitored and controlled appropriately by study personnel and veterinary staff.

Surgical procedures:

Surgeries were performed using aseptic technique on mice deeply anesthetized via inhalation of 2% isoflurane in O_2. Mice were placed on a warming pad for body temperature maintenance. The surgical field was prepared with hair trimmers and alternating passes of 10% povidone-iodine and 70% isopropanol. Under an operating microscope, the surgeon exposed the right tibial nerve using a longitudinal straight incision through the skin and dissection between the gluteal and quadriceps muscles. The sciatic nerve was freed from the surrounding tissue, and the tibial nerve separated from the fibular and sural nerve branches.

At this point, a space was cleared under the back skin over the supraspinal muscles using fine iris scissors (Fine Science Tools, Vancouver, Canada) and the implant coil was inserted. Prior to implantation, implants were sterilized under UV for 3 h per side. The nerve was fitted into the electrode cuff at the midpoint of the thigh. The tibial branch was transected 2 mm distal to the electrode cuff, then anastomosed using two 10–0 nylon (Roboz Surgical, Gaithersburg, MD) epineural stitches. Finally, the muscle was closed with 8–0 Vicryl suture and the skin closed with wound clips (Autoclip® system, Fine Science Tools).

Electrical stimulation:

Mice in wired-ES and wireless-ES treatment groups received one hour of ES under anesthesia, monitored both visually via paw twitching and electrophysiologically with a 30-gauge concentric needle EMG electrode (TE/B50600–001; Technomed USA Inc, White Bear Township, MN) connected with a clinical grade Nicolet EDX® system with Synergy software (Natus Neurology, Middleton, WI). For both wired and wireless devices, we delivered monophasic, 200 μsec pulses at 20Hz for one-hour duration, following previous reports with non-degradable stimulators.[3b, 29] For mice in the wired-ES group, the bioresorbable Mg electrodes and PLGA cuffs were disconnected from the external wires after the stimulation period, then implanted subcutaneously in a method and placement similar to the wireless device.

To verify and quantify ES delivery, CMAPs were recorded from the TA muscle, allowing adjustment of ES voltage in order to deliver supramaximal activation of the sciatic nerve. Supramaximal activation was further verified using SNAPs recorded from the 2nd toe. All recordings were made with concentric needle electrodes (TE/B50600–001; Technomed USA Inc).

Control mice received one hour of sham ES under anesthesia, with no current passed through their implants.

Retrograde tracing dye application:

At 21 days post-repair, mice were anesthetized and their tibial nerves exposed. The wound was irrigated with sterile saline and then dried with sterile cotton swab sticks. Tibial nerves were sharply cut 5 mm distal to the repair site and soaked in 10% Fluororuby dye (Dextran tetramethylrhodamine, D-1817, Invitrogen, Carlsbad, CA) on a 3 mm Gelfoam pad (Gelfoam® Absorbable Gelatin Sponge, Pfizer, New York City, NY) for 10 mins, then the wound was closed as described in Surgical Procedures. Mice were returned to their cages for 5 d to allow retrograde transport of the tracer to neuron somas in the spinal cord and dorsal root ganglia. In addition, seven uninjured mice underwent identical retrograde tracing to obtain baseline motor neuron counts for intact nerves.

Tissue handling:

Five days following retrograde labeling, mice were sacrificed and intracardially perfused with saline followed by 4% paraformaldehyde. Each animals' right hindlimb and spine were grossly dissected and immersed in 4% paraformaldehyde for 48 hours, and then further dissected to extract sciatic nerve and spinal cord. These tissues were immersed in 30% sucrose solution for 24–72 hours, and then snap-frozen in Tissue Freezing Material (TFM-C, Thermo Fisher Scientific) immersed in isopentane cooled by liquid nitrogen.

Spinal cords were harvested and serially sectioned into 40-μm-thick longitudinal sections on a cryostat (Leica Microsystems, Wetzlar, Germany) at −22°C. Tibial nerves were sectioned 2–3mm distal to the repair site in transverse sections 10 μm thick on the same machine. L5 DRGs were sectioned longitudinally in sections 8 μm thick on the same machine.

Tibial nerve axon quantification:

Tibial nerve sections were immunohistochemically stained with NeuroTrace 488nm (N21480, Invitrogen) and DAPI (F6057, Sigma Aldrich, St. Louis, MO) and imaged at 20x (Dmi8-S Inverted Microscope, Leica Microsystems). Images were captured at identical optical and camera settings and analyzed by an observer blinded to treatment group. ImageJ[28] was used to provide an automated measure of the area covered by labelled axons within the tibial perineurium. This was normalized against an unstained far red channel (647 nm) to control for variability in background autofluorescence.

Spinal motor neuron quantification:

Spinal cord sections were stained with DAPI (F6057, Sigma Aldrich) and imaged at 20x (Leica Dmi8-S Inverted Microscope System). All labeled neurons were hand-counted, and count accuracy was assessed by comparison with 15 randomly selected slides counted by a second blinded observer. Student's t-test showed no significant differences between counts obtained by different observers. Accurate estimations of individual labeled neuron count were calculated using Abercrombie's correction to account for duplicate counting of individual motor neuron nuclei.[30]

Dorsal root ganglia c-Fos staining:

L4–6 DRGs were obtained from mice one-hour post-treatment and stained with c-Fos antibody (ab190289, Abcam) and DAPI.

Statistical analysis:

An *a priori* power analysis (performed in G-Power 8/5/19) determined the number of animals needed to adequately power 1-way ANOVA comparison with an effect size of 0.5, α = 0.05.

For statistical analyses α level was set to 0.05. Results are expressed as mean values with standard error. Student's t-tests were used to compare sample means when two groups were involved, otherwise for multi-group comparisons one-way ANOVAs were used to determine the effects of treatment type on motor neuron count, distal axon regeneration, and other dependent outcome measures, followed by Fisher's LSD posthoc test. Sample Pearson correlation coefficient (r) was used to evaluate correlation between maximal wired and wireless CMAP and SNAP responses.

Supplementary Material

Refer to Web version on PubMed Central for supplementary material.

Acknowledgements

References

[1]. a)Noble J, Munro CA, Prasad VSSV, Midha R, Trauma J Acute Care Surg. 1998, 45, 116;b)Taylor CA, Braza D, Rice JB, Dillingham T, Am. J. Phys. Med. Rehabil. 2008, 87, 381; [PubMed: 18334923] c)Scholz T, Krichevsky A, Sumarto A, Jaffurs D, Wirth GA, Paydar K, Evans GRD, J. Reconstr. Microsurg. 2009, 25, 339; [PubMed: 19301234] d)Robinson LR, Muscle Nerve 2000, 23, 863. [PubMed: 10842261]

[2]. Portincasa A, Gozzo G, Parisi D, Annacontini L, Campanale A, Basso G, Maiorella A, Microsurgery 2007, 27, 455. [PubMed: 17596860]

[3]. a)Mar FM, Bonni A, Sousa MM, EMBO Rep. 2014, 15, 254; [PubMed: 24531721] b)Al-Majed AA, Neumann CM, Brushart TM, Gordon T, J. Neurosci 2000, 20, 2602; [PubMed: 10729340] c)Al-Majed AA, Brushart TM, Gordon T, Eur. J. Neurosci. 2000, 12, 4381. [PubMed: 11122348]

[4]. a)Al-Majed AA, Brushart TM, Gordon T, Eur. J. Neurosci. 2000, 12, 4381; [PubMed: 11122348] b)Al-Majed AA, Neumann CM, Brushart TM, Gordon T, The Journal of neuroscience : the official journal of the Society for Neuroscience 2000, 20, 2602; [PubMed: 10729340] c)Ward PJ, Jones LN, Mulligan A, Goolsby W, Wilhelm JC, English AW, PLoS One 2016, 11, e0154243; [PubMed: 27152611] d)Ward PJ, Clanton SL II, English AW, Eur. J. Neurosci. 2018, 47, 294. [PubMed: 29363200]

[5]. Lindsay RM, J. Neurosci. 1988, 8, 2394. [PubMed: 3249232]

[6]. Reichardt LF, Philos. Trans. R. Soc. 2006, 361, 1545.

[7]. Yao J, Sasaki Y, Wen Z, Bassell GJ, Zheng JQ, Nat. Neurosci. 2006, 9, 1265. [PubMed: 16980965]

[8]. a)Difato F, Tsushima H, Pesce M, Benfenati F, Blau A, Chieregatti E, Sci. Rep. 2011, 1, 183; [PubMed: 22355698] b)Inagaki N, Katsuno H, Trends Cell Biol. 2017, 27, 515. [PubMed: 28283221]

[9]. a)Brushart TM, Hoffman PN, Royall RM, Murinson BB, Witzel C, Gordon T, Neurosci J 2002, 22, 6631;b)Witzel C, Brushart TM, Koulaxouzidis G, Infanger M, J. Reconstr. Microsurg. 2016, 32, 491. [PubMed: 26975563]

[10]. Gordon T, Amirjani N, Edwards DC, Chan KM, Exp. Neurol. 2010, 223, 192. [PubMed: 19800329]

[11]. Power HA, Morhart MJ, Olson JL, Chan KM, Neurosurgery 2020, 86, 769. [PubMed: 31432080]

[12]. Wong JN, Olson JL, Morhart MJ, Chan KM, Ann. Neurol. 2015, 77, 996. [PubMed: 25727139]

[13]. Ray WZ, Mahan MA, Guo D, Guo D, Kliot M, Acta Neurochir. (Wien.) 2017, 159, 1765. [PubMed: 28500566]

[14]. Koo J, MacEwan MR, Kang SK, Won SM, Stephen M, Gamble P, Xie Z, Yan Y, Chen YY, Shin J, Birenbaum N, Chung S, Kim SB, Khalifeh J, Harburg DV, Bean K, Paskett M, Kim J, Zohny ZS, Lee SM, Zhang R, Luo K, Ji B, Banks A, Lee HM, Huang Y, Ray WZ, Rogers JA, Nat. Med. 2018, 24, 1830. [PubMed: 30297910]

[15]. a)Lee KY, Mooney DJ, Prog. Polym. Sci. 2012, 37, 106; [PubMed: 22125349] b)Reakasame S, Boccaccini AR, Biomacromolecules 2018, 19, 3. [PubMed: 29172448]

[16]. Kang S-K, Murphy RKJ, Hwang S-W, Lee SM, Harburg DV, Krueger NA, Shin J, Gamble P, Cheng H, Yu S, Liu Z, McCall JG, Stephen M, Ying H, Kim J, Park G, Webb RC, Lee CH, Chung S, Wie DS, Gujar AD, Vemulapalli B, Kim AH, Lee K-M, Cheng J, Huang Y, Lee SH, Braun PV, Ray WZ, Rogers JA, Nature 2016, 530, 71. [PubMed: 26779949]

[17]. Yin L, Cheng H, Mao S, Haasch R, Liu Y, Xie X, Hwang S-W, Jain H, Kang S-K, Su Y, Li R, Huang Y, Rogers JA, Adv. Funct. Mater. 2014, 24, 645.

[18]. a)Gao Y, Zhang Y, Wang X, Sim K, Liu J, Chen J, Feng X, Xu H, Yu C, Sci. Adv. 2017, 3, e1701222; [PubMed: 28879237] b)Poetz KL, Mohammed HS, Snyder BL, Liddil G, Samways DSK, Shipp DA, Biomacromolecules 2014, 15, 2573; [PubMed: 24848134] c)Yin L, Huang X, Xu H, Zhang Y, Lam J, Cheng J, Rogers JA, Adv. Mater. 2014, 26, 3879. [PubMed: 24652717]

[19]. Ng WF, Chiu KY, Cheng FT, Mater. Sci. Eng. C 2010, 30, 898.

[20]. Kang S-K, Koo J, Lee YK, Rogers JA, Acc. Chem. Res. 2018, 51, 988. [PubMed: 29664613]

[21]. Danckwerts P, Trans. Faraday Soc. 1950, 46, 300.

[22]. Fallegger F, Schiavone G, Lacour SP, Adv. Mater. 2020, 32, 1903904.

[23]. Choi YS, Koo J, Lee YJ, Lee G, Avila R, Ying H, Reeder J, Hambitzer L, Im K, Kim J, Lee K-M, Cheng J, Huang Y, Kang S-K, Rogers JA, Adv. Funct. Mater. 2020, 30, 2000941.

[24]. a)Singh B, Xu QG, Franz CK, Zhang R, Dalton C, Gordon T, Verge VM, Midha R, Zochodne DW, J. Neurosurg 2012, 116, 498; [PubMed: 22149377] b)Senger JB, Chan AWM, Chan KM, Kwan-Wong T, Acton L, Olson J, Webber CA, Neurorehabil. Neural Repair 2020, 34, 299. [PubMed: 32089098]

[25]. Lee G, Choi YS, Yoon H-J, Rogers JA, Matter 2020, 3, 1031.

[26]. a)Lee S, Koo J, Kang S-K, Park G, Lee YJ, Chen Y-Y, Lim SA, Lee K-M, Rogers JA, Mater. Today 2018, 21, 207;b)Won SM, Koo J, Crawford KE, Mickle AD, Xue Y, Min S, McIlvried LA, Yan Y, Kim SB, Lee SM, Kim BH, Jang H, MacEwan MR, Huang Y, Gereau IV RW, Rogers JA, Adv. Funct. Mater. 2018, 28, 1801819.

[27]. Franz CK, Puritz A, Jordan LA, Chow J, Ortega JA, Kiskinis E, Heckman CJ, Neurorehabilitation and neural repair 2018, 32, 735. [PubMed: 30043670]

[28]. Rasband WS, 1997–2018, ImageJ, U. S. National Institutes of Health, Bethesda, Maryland, USA, https://imagej.nih.gov/ij/.

[29]. a)Franz CK, Rutishauser U, Rafuse VF, Brain 2008, 131, 1492; [PubMed: 18334536] b)English AW, J. Comp. Neurol. 2005, 490, 427. [PubMed: 16127712]

[30]. Abercrombie M, Anat. Rec. 1946, 94, 239. [PubMed: 21015608]
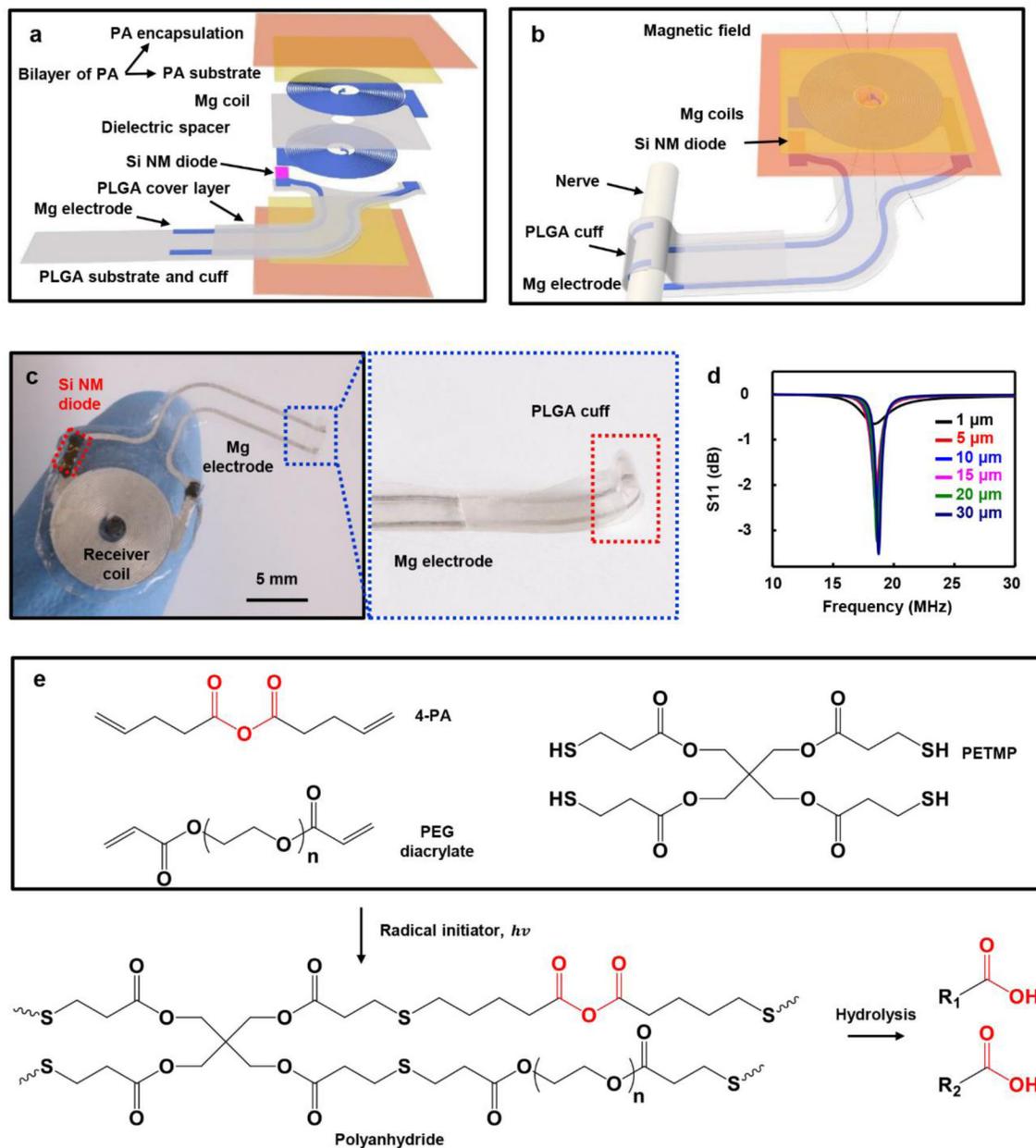
Figure 1.
Controlled-bioresorbable, wireless electrical stimulator. a) Exploded view schematic illustration of the device structure. b) Schematic illustration of the complete device, with nerve cuff interface. c) Image of a wireless electrical stimulator and magnified view of the hot-pressed PLGA cuff and Mg electrode. d) Electromagnetic simulation of the radio frequency behavior of the wireless electrical stimulator with various Mg thickness. e) Chemical components use to form the polyanhydride (PA) via UV initiated thiol-ene click reactions and the hydrolysis of anhydride. 4-PA: 4-pentenoic anhydride, PEG diacrylate: poly (ethylene glycol) diacrylate, PETMP: pentaerythritol tetrakis(3-mercaptopropionate).
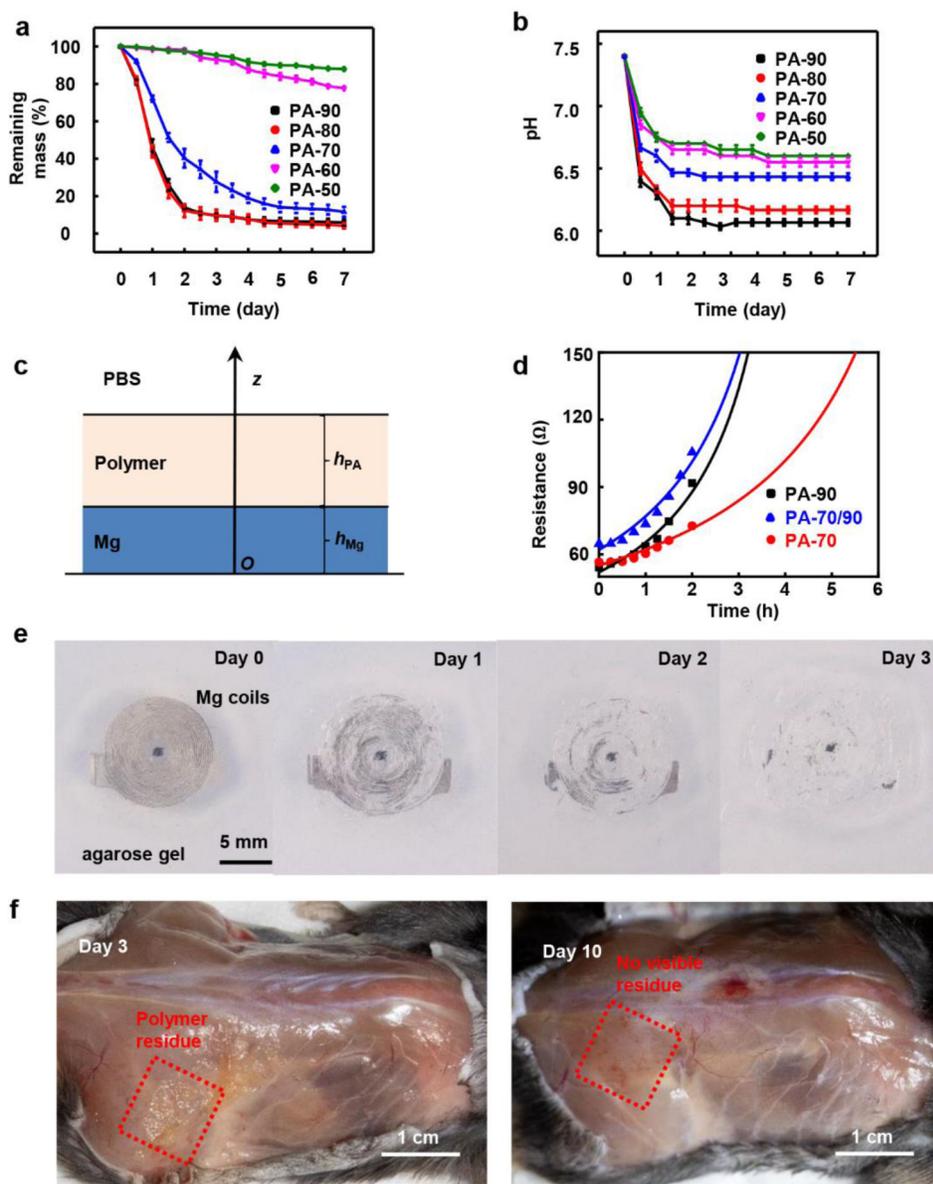
Figure 2.
Degradation properties of the polyanhydride film and electrical stimulator. a) Plot of remaining mass of various samples of polyanhydride ($20 \times 10 \times 0.05$ mm, ~10 mg) as a function of time of immersion in PBS at 37 ℃ and b) corresponding changes in the pH associated with the degradation process. c) Schematic illustration of the bilayer model of reactive diffusion. d) Theoretical (lines) and measured (dots) resistance changes of 300 nm thick Mg with the encapsulation of different polyanhydride layers barriers as a function of immersion time in PBS solution at 37 ℃. e) Images of Mg coils encapsulated in polyanhydride (PA-90 and PA-70) captured at different times after embedding the samples in agarose gel at 37 ℃. f) Photographs of the stimulator 3 and 10 days after implantation in the subcutaneous back region of a mouse model.
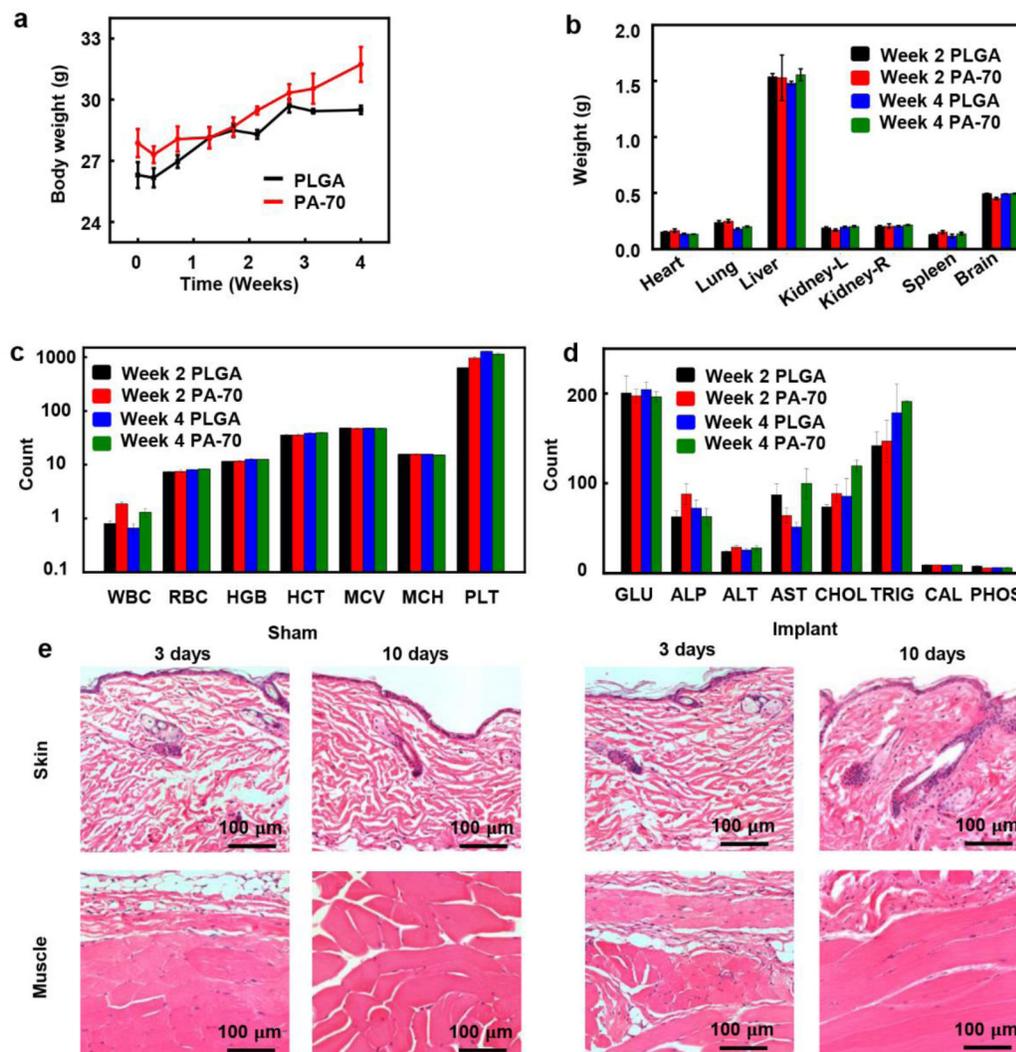
Figure 3.

In vivo evaluations of the biocompatibility of the polyanhydride materials and the wireless, electrical stimulator. a) Changes of body weight of mice in each group (control: PLGA, n=3 and PA-70, n=3). b) Comparison of weight of organs of mice in each group at two weeks and four weeks post-implantation (n=3). c, d) Blood counts and blood chemistry tests for mice in a) and b). ALP, alkaline phosphatase (U/L); ALT, alanine aminotransferase (U/L); AST, aspartate transaminase (U/L); CAL, calcium (mg/dL); CHOL, cholesterol (mg/dL); GLU, glucose (mg/dL); HCT, hematocrit level (%); HGB, blood hemoglobin level (g/dL); MCH, mean corpuscular hemoglobin (pg); MCV, mean corpuscular volume (fL); PHOS, phosphorus (mg/dL); PLT, platelet count in blood (×1,000/μL); RBC, red blood cell (×1,000,000/μL); TRIG, triglycerides (mg/dL); WBC, white blood cell (×1000/μL). (All data are shown as mean ± SEM) e) Images of histology of skin tissue and fascia/muscle tissue from mice with sham surgery and implanted device (encapsulated with a bilayer of PA-90 and PA-70) 3 days and 10 days post-surgery.
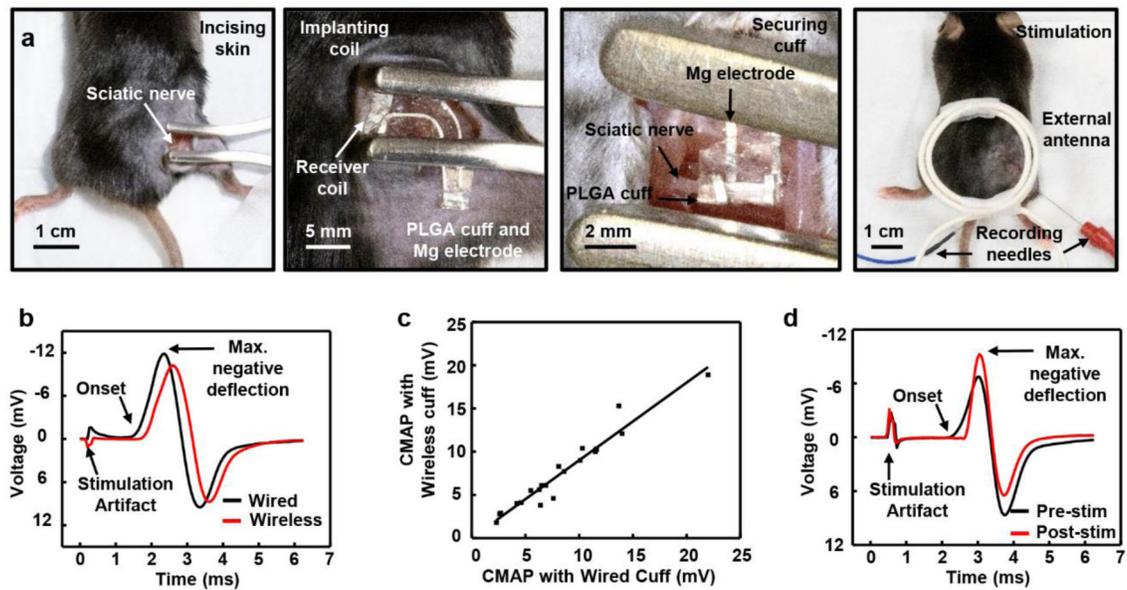
Figure 4.
Procedures for surgically implanting and operating bioresorbable, wireless electrical stimulators designed for the tibial nerve and results of in vivo tests. a) Surgical procedures. From left to right: incising the skin, implanting the receiver coil subcutaneously, securing the PLGA cuff and Mg electrode to the sciatic nerve, and suturing the incised skin, performing stimulation with an external antenna and attaching recording electrodes for CMAP monitoring. b) Maximum CMAP response from tibial anterior with wired electrical stimulation (21.4 mV) and wireless electrical stimulation (19.0 mV). c) Comparison of the maximum CMAP response from wired and wireless devices, showing the equivalence of the wireless and wired devices. d) Maximum CMAP response from the tibial anterior before (15.4 mV) and after (15.3 mV) one-hour wireless electrical stimulation.
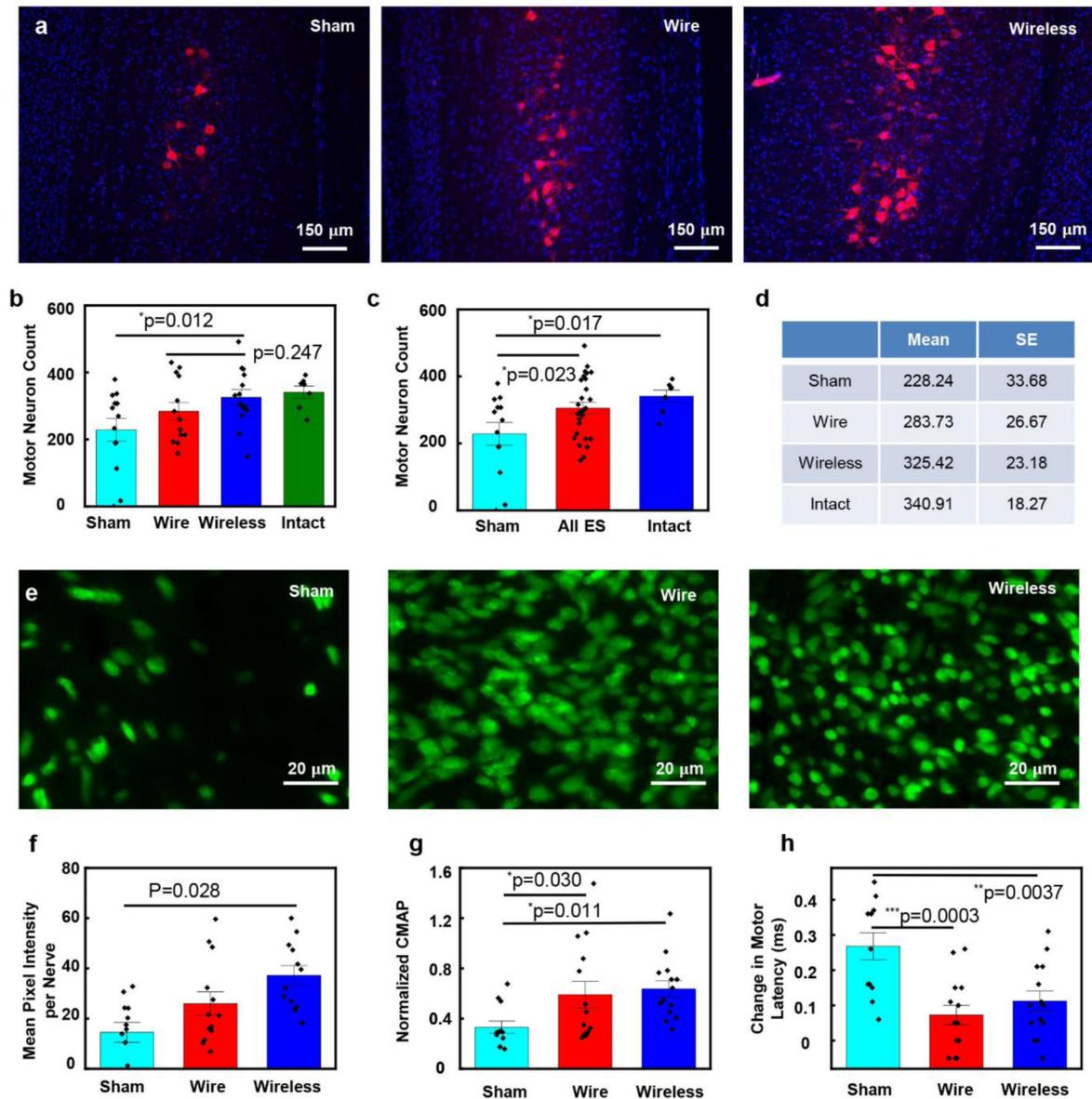
Figure 5.
Results of regeneration of transected nerves treated with one-hour of electrical stimulation delivered with wired and wireless devices, compared to no stimulation (sham). a) Representative images of spinal cord sections from three treatment groups. Red (590nm): retrogradely labelled motor neurons, Blue (460nm): DAPI, 4′,6-diamidino-2-phenylindole stained nuclei. b-d). Statistical analysis of motor neuron count results for the sham group (n=13), one-hour ES treatment group with wired device (n=13) and wireless device (n=14). Intact group (n=7). b) Wireless vs sham: *p=0.0122. Wireless vs wire: p=0.2474. c) Intact vs sham: *p=0.0166. ES vs sham: *p=0.0227. (D) Summary of the mean and SE of motor neuron count results for four groups. e) Representative images of distal nerve sections from three treatment groups. Green (488nm): regenerating axons. f) Statistical analysis of the distal axon growth. One-way ANOVA P=0.0281. g) Statistical analysis

of maximum negative peak CMAP amplitude at Day 21, normalized to intact. Sham: 0.3315±0.0486, wire: 0.5905±0.1055, wireless: 0.6363±0.0659. Wire vs: sham: *p=0.0295. Wireless vs sham: *p=0.0114. Wireless vs wire: *p=0.6795. h) Statistical analysis of change in motor latency at Day 21 compared to before injury. Sham: 0.2675 ± 0.0384 ms, wire: 0.0729±0.0275 ms, wireless: 0.1121±0.0282 ms. Wire vs: sham: [***]p=0.0003. Wireless vs sham: [**]p=0.0037. Wireless vs wire: p=0.6342. The data are shown as mean ± SEM.